Research Paper

High-voltage lithium-metal battery with three-dimensional mesoporous carbon anode host and ether/carbonate binary electrolyte

Egy Adhitama [a], Purna Chandra Rath [a], Achmad Prayogi [a], Jagabandhu Patra [a, b], Tai-Chou Lee [c], Ju Li [d], Jeng-Kuei Chang [a, b, *]

[a] Department of Materials Science and Engineering, National Yang Ming Chiao Tung University, 1001 University Road, Hsinchu 30010, Taiwan
[b] Hierarchical Green-Energy Materials (Hi-GEM) Research Center, National Cheng Kung University, 1 University Road, Tainan, 70101, Taiwan
[c] Department of Chemical and Materials Engineering, 300 Jhong-Da Road, National Central University, Taoyuan, 32001, Taiwan
[d] Department of Nuclear Science and Engineering and Department of Materials Science and Engineering, Massachusetts Institute of Technology, 77 Massachusetts Ave, Cambridge, MA, 02139, USA

ARTICLE INFO

ABSTRACT

Electrolyte recipes and Li metal anode host materials are developed for lithium-metal batteries. 1,2-dimethoxyethane/ethylene carbonate mixed solvent with 1 M lithium bis(fluorosulfonyl)imide and 1 wt% $LiNO_3$ is shown to form a robust solid electrolyte interphase and improve Coulombic efficiency and cyclability during Li metal plating/stripping. This electrolyte can withstand high potential, allowing the operation of a $LiNi_{0.8}Co_{0.1}Mn_{0.1}O_2$ (NMC-811) cathode. One-dimensional carbon nanotubes, two-dimensional graphene nanosheets, and three-dimensional ordered mesoporous carbon CMK-8 are used as the host materials for the accommodation of Li metal. The strong and continuous conducting network of CMK-8 with interpenetrating open channels is found to be a promising scaffold for Li metal. With the proposed electrolyte, the CMK-8 electrode enables uniform Li plating/stripping with a high Coulombic efficiency of 99.2% under a practical current density of 1 mA cm^{-2}. Moreover, a long life of >550 charge-discharge cycles is achieved. The high structural stability of CMK-8 upon cycling is confirmed using electron microscopy and Raman spectroscopy. Finally, we use a Li-free CMK-8 electrode, an NMC-811 cathode, and the proposed electrolyte to construct a full cell. The electrochemical properties are evaluated.

1. Introduction

Batteries have a broad range of applications, from portable electronic devices to electric vehicles and power grid systems, and are thus extensively researched. The performance of Li-ion batteries (LIBs), the state of the art in electrochemical energy storage, is approaching a plateau. Improvements that result in higher energy density are required. A promising approach to improve performance is to replace the graphite anode of LIBs with a Li metal anode [1], which has an extremely high theoretical capacity (3860 mAh g^{-1}) and low electrochemical redox potential (−3.040 V vs. standard hydrogen electrode) [2]. However, the practical implementation of a Li anode is hindered by an unstable interface that stems from the high reactivity between Li metal and the electrolyte, leading to low Coulombic efficiency (CE), Li dendrite formation, and even safety concerns. To overcome these problems, more research is required on the electrolyte composition design and Li anode architecture optimization.

Lithium bis(trifluoromethanesulfonimide) (LiTFSI) salt in 1,3-dioxolane (DOL)/1,2-dimethoxyethane (DME) solvent with $LiNO_3$ as an additive is a typical electrolyte used for Li metal anodes [3—7] owing to its lower reduction potential than that of carbonate-based electrolytes [8] and low reactivity with Li metal [9]. This ether-based electrolyte is promising because a polymer passivation layer forms when it decomposes on the Li surface; this layer ensures high CE during Li plating/stripping [10] and provides high elasticity, suppressing Li dendrite growth [11]. However, this kind of electrolyte is incompatible with many LIB cathodes due to its insufficient anodic decomposition potential (i.e., <4 V vs. Li$^+$/Li). For example, the high-capacity Ni-rich $LiNi_{0.8}Mn_{0.1}Co_{0.1}O_2$ (NMC-811) cathode usually requires a charge cut-off potential of ≥4.2 V [12].

* Corresponding author. 1001 University Road, National Yang Ming Chiao Tung University, Hsinchu, Taiwan.
E-mail address: jkchang@nctu.edu.tw (J.-K. Chang).

Thus, operation of the NMC-811 cathode in the DOL/DME ether-based electrolyte is infeasible, significantly limiting battery energy density [13]. In contrast, a carbonate-based electrolyte, which has great high-voltage cathode compatibility and is thus commonly used for conventional LIBs, does not form a robust solid electrolyte interphase (SEI) on the Li anode [8]. Repeated Li plating/stripping can lead to pronounced Li dendrite formation [12]. Moreover, the severe side reactions on Li result in a low CE (usually <80%) [14,15]. An electrolyte recipe that can meet the requirements of a Li anode and a high-voltage cathode is thus highly desirable.

The large volume change of a Li metal anode during electroplating/stripping is the main reason for electrode/electrolyte interface instability. The electrode volume expansion/contraction makes the SEI mechanically unstable [3,16]. The repeated breakdown and regeneration of the SEI continuously consume cyclable Li and the electrolyte and thicken the SEI upon cycling, increasing interface resistance. Moreover, nanoscale defects in the SEI can cause locally concentrated Li^+ flux, leading to Li dendrite growth [17—20]. It has been reported that unreacted Li that is disconnected from the current collector and/or encapsulated by the insulating SEI is mainly responsible for the capacity loss of a Li electrode [21]. Therefore, structural connections crucially affect Li anode performance. Effective electronic conduction pathways that minimize isolated Li are the key. Nanostructured carbon materials are promising scaffolds for hosting Li at the anode of lithium-metal batteries (LMBs) to overcome the above problems [22]. Multilayer graphene [23], crumpled graphene [5], and a graphene/carbon nanotube (CNT) hybrid [24] have been adopted for this task. Unfortunately, graphene materials easily aggregate and can break or collapse during cycling [25,26]. Hollow silica microspheres with a CNT core have been fabricated to host Li and prevent dendrite formation [27]. However, their synthesis is complicated and this architecture can be fragile. The drawbacks of previously reported carbon hosts include insufficient CE during Li plating/stripping, unfavorable Li^+ transport due to high tortuosity of micropores, and the unsatisfactory cyclability associated with the disintegration of the host materials [28]. The design of carbon hosts with optimal architecture, pore geometry and tortuosity, and structural connectivity is our research target.

In the first part of this study, an electrolyte recipe is developed to increase the CE and cycling stability of the Li plating/stripping reaction and achieve a large potential window to allow the operation of an NMC-811 cathode. In the second part, one-dimensional (1-D) CNT, two-dimensional graphene (2-D), and three-dimensional (3-D) ordered mesoporous carbon CMK-8 host materials (for Li metal) are systematically compared. We first show that CMK-8, which has unique bicontinuous electronic and ionic conduction pathways and ordered meso-size 3-D open channels, is a highly promising scaffold for LMB anodes. The functions of CMK-8 include the dissipation of Li plating/stripping current, confinement of the deposited Li, dimensional stabilization of the electrode/electrolyte interface, construction of a 3-D conduction framework within the Li electrode, and creation of a proper porosity for Li^+ transport. Finally, we combine the proposed electrolyte and the CMK-8 host material to assemble a Li-metal-free full cell with an NMC-811 cathode. Promising charge-discharge performance is demonstrated.

2. Experimental section

2.1. Materials preparation

Ordered silica KIT-6 was synthesized and used as the hard template to fabricate CMK-8. KIT-6 was prepared following a previously reported method [29]. For the nanocasting of carbon into KIT-6, 10 g of KIT-6 and 12.5 g of sucrose (as the carbon precursor) were dispersed in 30 g of deionized water. Then, 1.5 g of H_2SO_4 was added dropwise to trigger carbon precipitation. The mixture was dried at 100 °C for 8 h and then at 160 °C for another 24 h. The obtained powder was carbonized at 900 °C for 3 h under an Ar atmosphere. The KIT-6 template was removed using 2 M NaOH solution at 90 °C for 24 h. After repeated washing with deionized water and drying at 70 °C, CMK-8 was obtained. Graphene nanosheets were synthesized according to our previously reported method [30]. Multi-walled CNTs were purchased from CNTouch Co. Ltd.

2.2. Materials characterization

The microstructures of the samples were characterized using scanning electron microscopy (SEM, HITACHI S-2500) and transmission electron microscopy (TEM, JEOL JEM-F200). X-ray diffraction (XRD) patterns were recorded with a Bruker D2 PHASER diffractometer to identify the phases in the samples. A Raman spectrometer (LabRAM HR-800) was used to study the carbon bonding characteristics. A diode-pump solid-state laser with a wavelength of 532 nm was adopted. The N_2 adsorption/desorption isotherm measurements were conducted at −196 °C using a Micromeritics ASAP 2020 analyzer. The specific surface area was calculated using the Brunauer-Emmett-Teller (BET) method. X-ray photoelectron spectroscopy (XPS, VG Sigma Probe) was employed to examine the surface chemical composition of the electrodes. The cycled electrodes were rinsed with electrolyte solvent and dried in an argon-filled glove box before being transferred to the XPS analysis chamber.

2.3. Electrochemical measurements

Battery-grade LiTFSI, lithium bis(fluorosulfonyl)imide (LiFSI), DOL, DME, ethylene carbonate (EC), and lithium nitrate ($LiNO_3$) were used. The solvents were dried over fresh molecular sieves for two days before use. 1 M LiFSI in EC/DME mixed solvent (with an EC/DME volume ratio of 1:1) with 1 wt% $LiNO_3$ was stirred for 24 h to ensure uniformity. The commonly used 1 M LiTFSI DOL/DME (with a volume ratio of 1:1) with 1 wt% $LiNO_3$ electrolyte was also prepared for comparison. The Li salt solubility in both electrolytes was found to be ~7 M. 1-D CNT, 2-D graphene, and 3-D CMK-8 were used as the host materials for Li plating/stripping. Each material was mixed with Super P and polyvinylidene fluoride (PVDF) binder (with a mass ratio of 7:2:1) in N-methyl-2-pyrrolidone (NMP) solution using a Thinky ARE-310 mixer. The obtained slurry was coated onto Cu foil and dried in a vacuum oven at 90 °C for 6 h. The material mass loading was typically 2.5—3 mg cm^{-2} with a coating thickness of ~30 μm. A contact angle goniometer was used to examine the electrolyte wettability toward various electrodes. For the Li plating/stripping experiments, three conditioning cycles were performed with a current density of 0.2 mA cm^{-2}. A multi-channel electrochemical workstation (Biologic VSP-300) was utilized to conduct the chronopotentiometry tests. LiFePO$_4$ (MTI Corp.) and NMC-811 (UBIQ Technology Co. Ltd.) cathodes were used. The cathode slurry was prepared with 70 wt% active material, 20 wt% Super P, and 10 wt% PVDF in NMP solution. The mass loading on the Al current collector was ~10 mg cm^{-2}. The electrodes were punched to match the required dimensions of a CR2032 coin cell. The electrolyte preparation and coin cell assembly were performed in an argon-filled glove box (Vigor Tech. Co. Ltd.), where both the moisture and oxygen content levels were below 0.3 ppm. The electrolyte amount was fixed at 60 μL for every coin cell. The charge-discharge properties (such as capacity, rate capability, and cycling stability) of the cells were evaluated at 25 °C using an Arbin BT-2043 battery tester.

3. Results and discussion

First, the conventional 1 M LiTFSI DOL/DME with 1 wt% LiNO$_3$ (denoted as LDD) electrolyte and 1 M LiFSI EC/DME with 1 wt% LiNO$_3$ (denoted as LED) electrolyte were compared. The ionic conductivity values of the LDD and LED electrolytes are 7.21 and 9.76 mS cm^{-1}, respectively. Fig. 1a and b shows the Li plating/stripping curves of Li//Cu cells measured at various current densities. Generally, the LDD cell exhibited a higher polarization than that of the LED cell, especially at high current densities. The lower overpotential for the latter cell can be attributed to higher ionic conductivity and lower electrode/electrolyte interfacial resistance. The obtained CE values under various rates for both electrolytes are shown in Table S1. At a current density of 1 mA cm^{-2}, the LDD and LED cells showed Li plating/stripping CE values of 97.7% and 98.7%, respectively. The CE values for the LDD cell decayed quickly with increasing current density (e.g., 28.7% @10 mA cm^{-2}), whereas those for the LED cell were relatively steady, even at a high rate (e.g., ~90.0% @10 mA cm^{-2}). In addition to the higher electrolyte conductivity, the superior CE for the LED cell is associated with the highly conductive and thin SEI layer derived from the FSI$^-$ anions [31]. A synergy between DME and LiFSI, but not LiTFSI, has been reported to form a robust SEI [11]. In addition, EC is prone to form a protective SEI layer on the electrode surface [31]. In contrast, the easy ring-opening polymerization of DOL can cause irreversible consumption of Li$^+$ and an increase in interface resistance [32,33], resulting in efficiency loss.

In Fig. 1a, the Li plating process of the LDD cell shows two distinct potential plateaus at high current densities. The potential drop is associated with an increase in the interfacial resistance at the Li counter electrode. At the Li side, the deposited Li in the previous cycle was completely consumed right before the point of the potential drop. The untapped Li underneath, which needed a higher overpotential to overcome the interface energy barrier, was then dissolved. In contrast, the LED cell did not exhibit a stepped potential drop. This confirms that the LED electrolyte allows better Li plating/stripping reversibility with lower SEI resistance.

The Li plating/stripping cycling stability of the Li//Cu cells with the two electrolytes was evaluated. Fig. 1c and d shows the data recorded at current densities of 1 and 5 mA cm^{-2}, respectively, with an areal capacity of 1 mAh cm^{-2}. For the LDD cell, the CE started to decay after ~45 and ~5 cycles at 1 and 5 mA cm^{-2}, respectively. The CE drop and rebound at high rate can be ascribed to the unstable electrode/electrolyte interface. The formed Li dendrites could occasionally connect and then dis-connect two electrodes during Li deposition/stripping, leading to the CE instability [5,34]. In contrast, the superior cyclability of the LED cell was shown up to 150 cycles with average CE values of 97.7% (at 1 mA cm^{-2}) and 92.9% (at 5 mA cm^{-2}). Fig. S1 in the Supporting Information shows the galvanostatic cycling stability of the Li//Li symmetric cells with the two electrolytes. The symmetric cells were tested under a current density of 5 mA cm^{-2} with each cycle having 1 mAh cm^{-2} of Li plating and stripping. As shown, the polarization of the LDD cell increases and fluctuates with increasing cycle number. The cell short-circuited after ~95 cycles. In contrast, the cell with the LED electrolyte had little change in terms of polarization upon cycling, even under such a high current density. No short-circuit failure was observed up to 350 cycles.

To examine the SEI chemistry, which is crucial for battery performance [35,36], XPS analysis was carried out on the Cu electrodes that had been (Li plating/stripping) cycled three times in the LDD and LED electrolytes. Fig. 2a and b shows the C 1s, O 1s, and F 1s spectra of the electrodes. The C 1s spectra can be split into four distinct signals. The peaks located at 284.8, 286.5, 288.2, and 290.4 eV can be ascribed to C–C, C–O, R–CO$_3$, and Li$_2$CO$_3$ bonds,

respectively [37,38]. The SEI that formed in the LED electrolyte has higher concentrations of polar R–CO$_3$ and Li$_2$CO$_3$ species, which have been reported to facilitate Li$^+$ transport [39,40]. The O 1s spectra contain LiOH (at 531.2 eV), Li$_2$CO$_3$ (at 532.9 eV), and –(CH$_2$–CH$_2$–O)$_n$– (at 533.5 eV) components. The LED-derived SEI is enriched with Li$_2$CO$_3$, which is mechanically robust [41]. The inorganic Li$_2$CO$_3$ is mainly distributed near the anode surface and acts as a junction to connect outer organic SEI species for stabilization of electrode interface [42]. In addition, Li$_2$CO$_3$ is insoluble in the electrolyte and is an electronic insulator, leading to a great passivation ability [42,43]. Conversely, LiOH and –(CH$_2$–CH$_2$–O)$_n$– moieties are known to impede Li$^+$ conduction [44]. The large amounts of these species in the LDD-derived SEI could hinder Li plating/stripping, deteriorating CE. The F 1s spectrum of the LDD sample consists of a relatively weak signal at 684.8 eV, which is related to LiF, and a strong signal at ~688.0 eV, which is related to C–F bonding [38]. The latter signal is associated with a moiety of the LiTFSI salt [45]. Stable LiTFSI is not readily decomposed [45]; thus, a less protective SEI was formed. In contrast, the LED spectrum shows only a strong LiF peak (no C–F signal appears). The complete decomposition of LiFSI promotes the formation of a high concentration of LiF, which is electrochemically stable and believed to be a good electronic insulator that can passivate the Li surface and prevent excessive electrolyte consumption [46]. The high fractions of both LiF (for decreasing electronic conduction) and Li$_2$CO$_3$ (for increasing mechanical strength) in the SEI are highly desirable and are responsible for the superior CE during Li plating/stripping, rate capability, and cycling stability for the LED electrolyte.

We assembled anode-free cells with the LiFePO$_4$ cathodes using the two electrolytes. Bare Cu foil was used on the negative-electrode side. Fig. S2 shows the obtained data measured at a rate of 1 C (based on LiFePO$_4$). In this anode-free configuration, Li$^+$ ions are obtained from the cathode side and transferred onto the Cu current collector as metallic Li during cell charging. The Li is stripped and transferred back to the cathode in the following discharge process [47,48]. Accordingly, the electrolyte recipe that affects the Li plating/stripping CE is crucial to determine the cell cycle life. As shown, the LDD cell retained only 10% of its initial capacity after 60 charge-discharge cycles, whereas the LED cell retained ~43% of its initial capacity after the same number of cycles.

The anodic stability of the two electrolytes was evaluated using linear sweep voltammetry (LSV) with Li/Al cells. Fig. 3a shows the data acquired at a potential sweep rate of 1 mV s^{-1}. The LDD and LED electrolytes began to show an irreversible oxidation current at ~4.1 and ~4.5 V, respectively. Fig. 3b and c compares the charge-discharge curves of NMC-811 half cells with the electrolytes. The charging voltage of the LDD cell can hardly reach 4.2 V. A voltage plateau was observed, reflecting electrolyte decomposition. The accumulated decomposition product layer may breakdown and lead to the voltage drop. Notably, successful operation and high charge-discharge capacities were achieved for the LED cell up to 4.45 V (cell failure occurred at 4.5 V). The superior anodic stability of the LED electrolyte can be attributed to the strong cathode electrolyte interphase that forms via the synergistic interaction between LiFSI and DME [49]. Moreover, the EC solvent has a lower highest occupied molecular orbital energy level than that of DOL, resulting in a higher decomposition potential. The above results indicate that the proposed LED electrolyte is promising for high-voltage LMB applications.

With the LED electrolyte, the properties of various carbon host materials (1-D CNTs, 2-D graphene, 3-D CMK-8) were assessed. The morphologies of the carbonaceous materials were inspected using SEM (Fig. S3) and TEM (Fig. 4). The outer and inner diameters of the multi-walled CNTs are approximately 15 and 5 nm, respectively. The CNT length is up to several micrometers. The lateral size of the
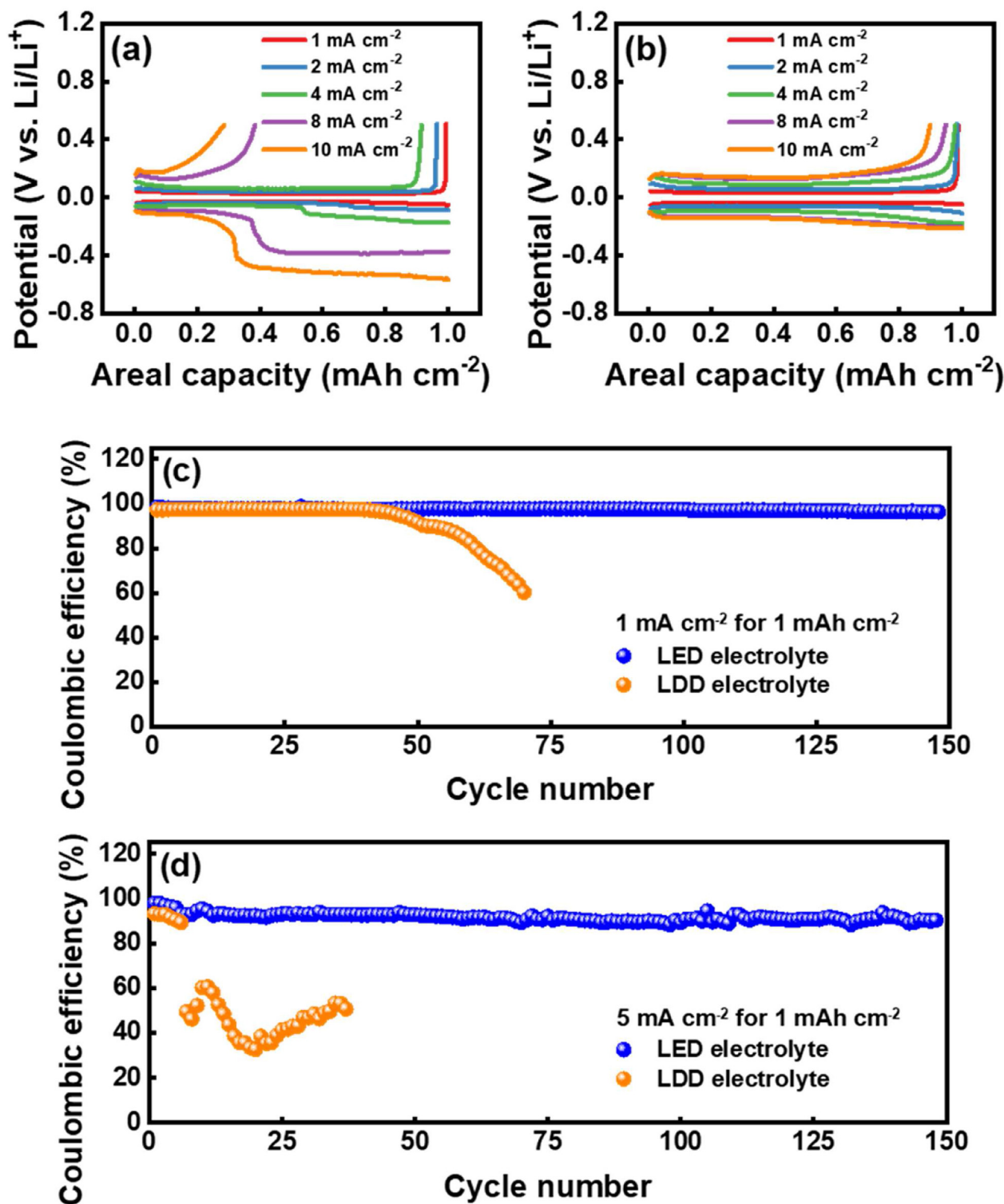
Fig. 1. Li plating/stripping curves of Li//Cu cells measured at various current densities with (a) LDD and (b) LED electrolytes. The CE vs. cycle number profiles of the two cells tested at (c) 1 mA cm^{-2} and (d) 5 mA cm^{-2} with areal capacity of 1 mAh cm^{-2}. (A colour version of this figure can be viewed online.)

graphene flakes is a few micrometers. The high electron transparency of the graphene TEM image indicates that the graphene sheets were well-exfoliated and composed of only a few carbon layers. The micrograph of CMK-8 shows a long-range ordered porous structure. The pore size is approximately 5 nm. The continuous carbon framework can provide electronic conduction and is known for its structural robustness [29]. The BET surface area values for the CNTs, graphene, and CMK-8 are 150, 585, and 1100 m^2 g^{-1}, respectively.

Fig. 5a–c shows the Li plating/stripping curves of the 1-D CNT, 2-D graphene, and 3-D CMK-8 electrodes, respectively, recorded at various current densities. As demonstrated, the polarization of the
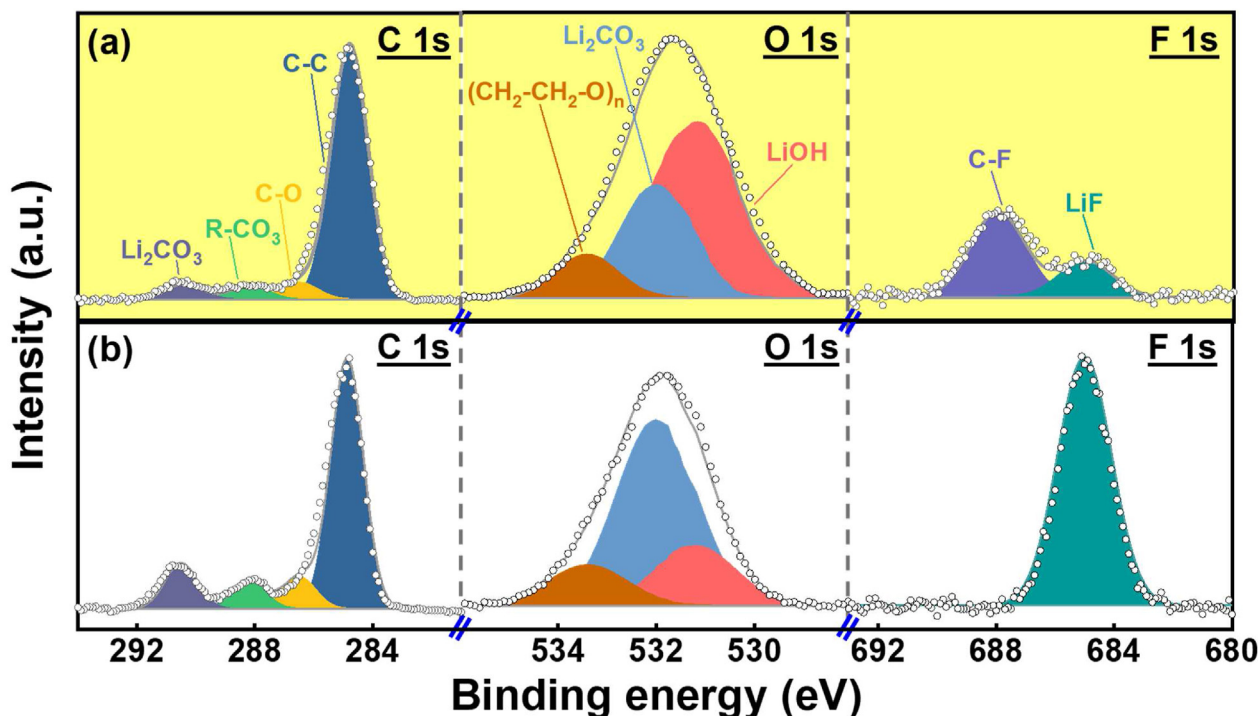
Fig. 2. XPS spectra of SEI layers derived from (a) LDD and (b) LED electrolytes on Cu electrodes. (A colour version of this figure can be viewed online.)

CMK-8 electrode is lower than those of the former two electrodes. This is related to CMK-8 having the highest BET area, allowing it to best dissipate the current. The obtained CE values of various electrodes are listed in Table S2. For the CMK-8 electrode, the CE at 1 mA cm^{-2} is as high as 99.2%. For a 4-mAh cm^{-2} practical cell, this rate is equal to 0.25C. Even at a high current density of 8 mA cm^{-2}, the CE value is 96.5%. These values are considerably higher than those for the CNT and graphene electrodes. Fig. 5d compares the cycling stability of Li plating/stripping for various carbon electrodes. At 1 mA cm^{-2}, the CE of the CNT and graphene electrodes began to significantly decay at the ~190th and ~70th cycles, respectively. The CMK-8 electrode showed stable operation up to 550 cycles with an average CE of ~98.4%. The stable CMK-8 framework provides 3-D continuous electronic and ionic conduction pathways [50], leading to the high CE and great cyclability. The performance difference between the three kinds of carbon electrodes became even more pronounced at 5 mA cm^{-2}, as shown in Fig. 5e. It is noted that even at such a high current density, the CMK-8 electrode showed steady charge-discharge performance up to 300 cycles. Table S3 compares the cycling stability of various carbon-based host materials reported in the literature. As can be seen, the 3-D CMK-8 electrode is one of the best anode hosts for LMBs.

The detailed Li metal plating/stripping profiles of the three carbonaceous host electrodes upon cycling at 1 mA cm^{-2} are shown in Fig. 5f. For the CNT and graphene electrodes, large fluctuations of the Li plating and stripping overpotentials can be observed. After 380 and 140 h, respectively, internal short-circuiting occurred. The 3-D CMK-8 electrode had a much longer lifetime (up to 1100 h). These results suggest that an unstable, resistive SEI with an uncontrolled Li morphology formed at the CNT and graphene electrodes, whereas a favorable Li/electrolyte interface with reduced side reactions upon cycling formed at the CMK-8 electrode.

Fig. 6a–d shows SEM images of plain Cu, CNT, graphene, and CMK-8 electrodes, respectively, before and after Li plating/stripping

cycling. The morphologies of the electrodes with deposited Li (1 mA cm^{-2} for 1 mAh cm^{-2}) and after Li was stripped at the 70th cycle are compared. We observed that moss-like Li was deposited on the plain Cu current collector (Fig. 6a). In the stripping state, a lot of residues were left, which is ascribed to the "dead" Li and thick SEI that accumulates during repeated cycling. As shown in Fig. 6b, the randomly stacked CNTs (with relatively small surface area) cannot regulate the growth of deposited Li. There is only "point constant" between CNTs, and thus a continuous electronic conduction network is hard to be established. As a consequence, Li filaments were deposited. After stripping, some dead Li filaments remained, and the CNT network was damaged. The XRD data in Fig. S4 show that the graphitic diffraction peaks of CNTs clearly diminished after cycling. Repeated high-degree lithiation and fast delithiation deteriorated the CNT crystallinity and destroyed the tubular structure. Thus, CNTs are not a good candidate for hosting Li in LMBs. Fig. 6c shows that uneven metallic Li was deposited on the outer surface of graphene and in the gaps between the graphene flakes. Similar to 1-D CNTs, 2-D graphene is unable to control the Li morphology. Because most of the Li was exposed to the electrolyte (rather than being confined in the carbon host), more side reactions occurred, leading to a lower CE (see Table S2). Upon Li stripping, the graphene sheets became highly pulverized. The structural robustness was found to be inferior to that of CNTs. The breakdown of the graphene sheets collapsed the host architecture and disconnected the electronic conduction pathways. This resulted in the graphene electrode having the worst cycling stability, as shown in Fig. 5d and e.

As shown in Fig. 6d, after Li metal plating, the surface of the CMK-8 electrode is relatively clean, suggesting that the Li mainly infiltrated the CMK-8 mesopores. For 3-D CMK-8, the high surface area dissipates the current, the interpenetrating open channels ensure effective Li$^+$ transport, and the continuous carbon skeleton establishes an electronic conduction framework. Owing to the capillary effects [51,52], most of the Li was deposited and confined
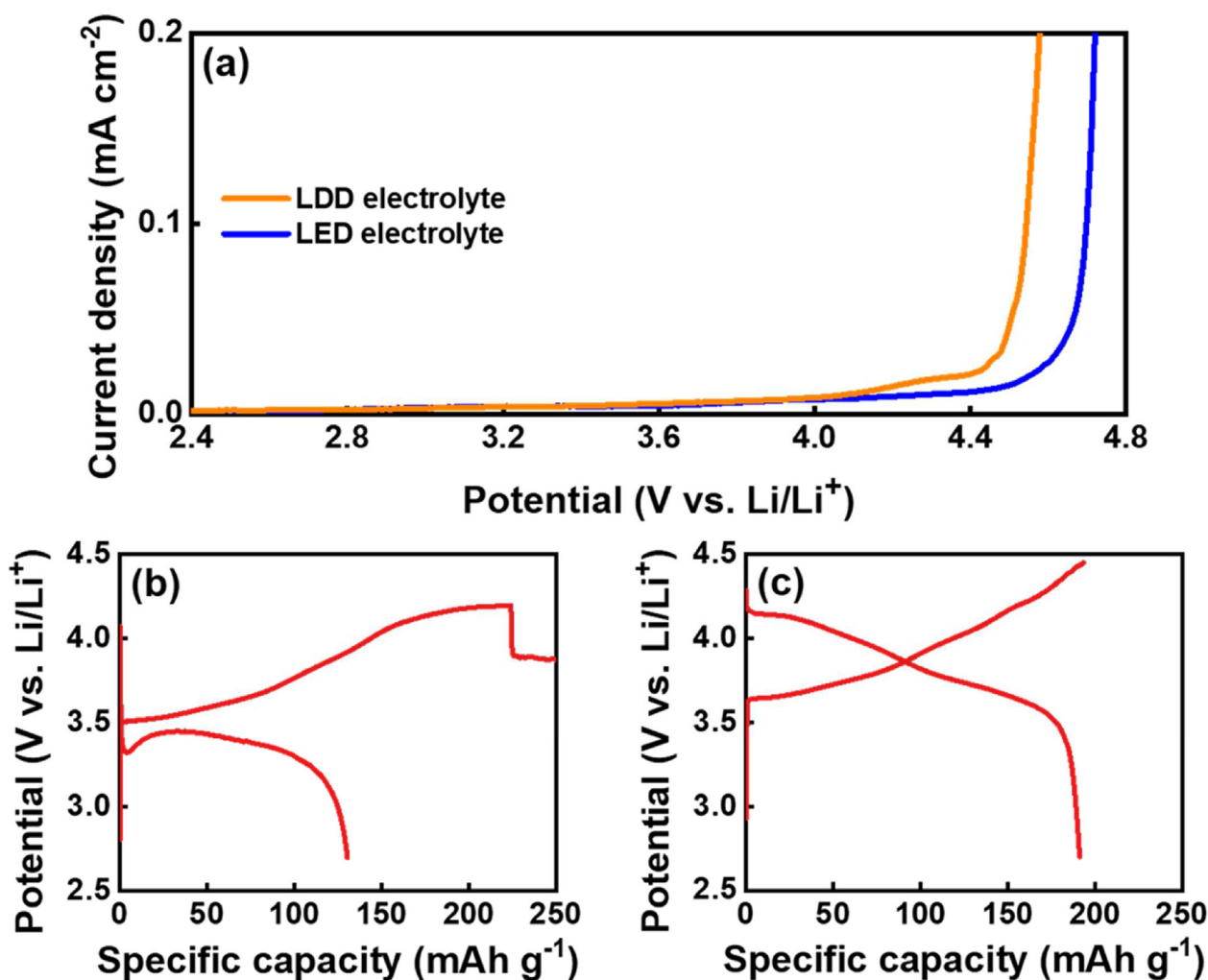
Fig. 3. (a) LSV curves of Al electrodes recorded in LDD and LED electrolytes. Charge-discharge curves of NMC-811 half cells measured at 0.1C with (b) LDD and (c) LED electrolytes. (A colour version of this figure can be viewed online.)
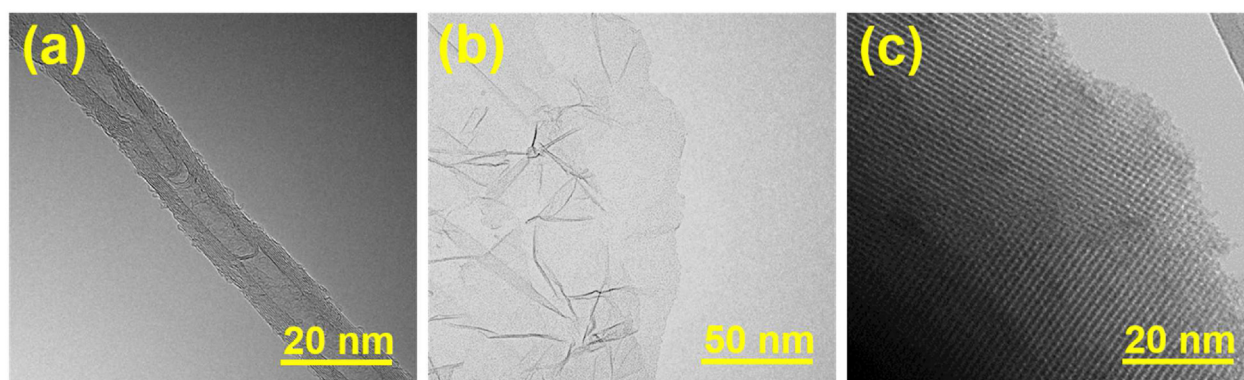

Fig. 4. TEM images of (a) 1-D CNTs, (b) 2-D graphene, and (c) 3-D CMK-8. (A colour version of this figure can be viewed online.)

within the mesoporous CMK-8 (rather than on the electrode surface), minimizing the Li dendrite formation. The excellent wettability of the CMK-8 electrode with the electrolyte is shown in Fig. S5. After Li stripping, there was almost no change in the electrode morphology compared to that of the fresh CMK-8 electrode, except the formation of a uniform surface SEI layer. The 3-D continuous conduction network of CMK-8 minimized the residual dead Li on the electrode. Moreover, the robust CMK-8 scaffold acted as a dimensional stabilizer that ensured electrode/electrolyte interface stability. Accordingly, a high CE and great cycling stability of the CMK-8 electrode for hosting Li was achieved, as demonstrated in Fig. 5.

The structural robustness of various carbonaceous host materials was further evaluated using Raman spectroscopy. Fig. 7a–c
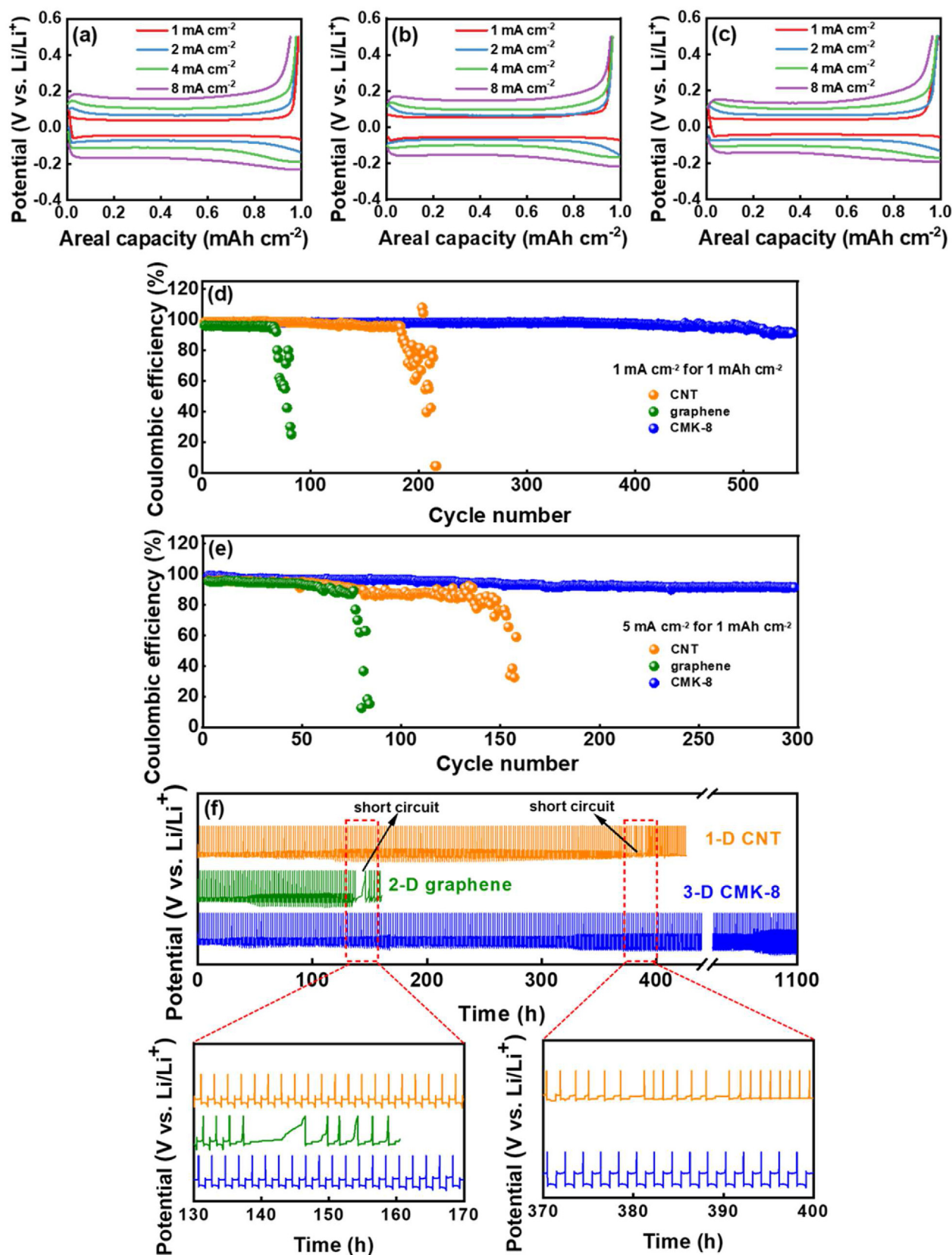
Fig. 5. Li plating/stripping curves of (a) 1-D CNT, (b) 2-D graphene, and (c) 3-D CMK-8 electrodes measured at various current densities. The CE vs. cycle number profiles of the three electrodes tested at (d) 1 mA cm^{-2} and (e) 5 mA cm^{-2} with areal capacity of 1 mAh cm^{-2}. (f) Li plating/stripping potential profiles of various electrodes measured at 1 mA cm^{-2} with areal capacity of 1 mAh cm^{-2}. (A colour version of this figure can be viewed online.)
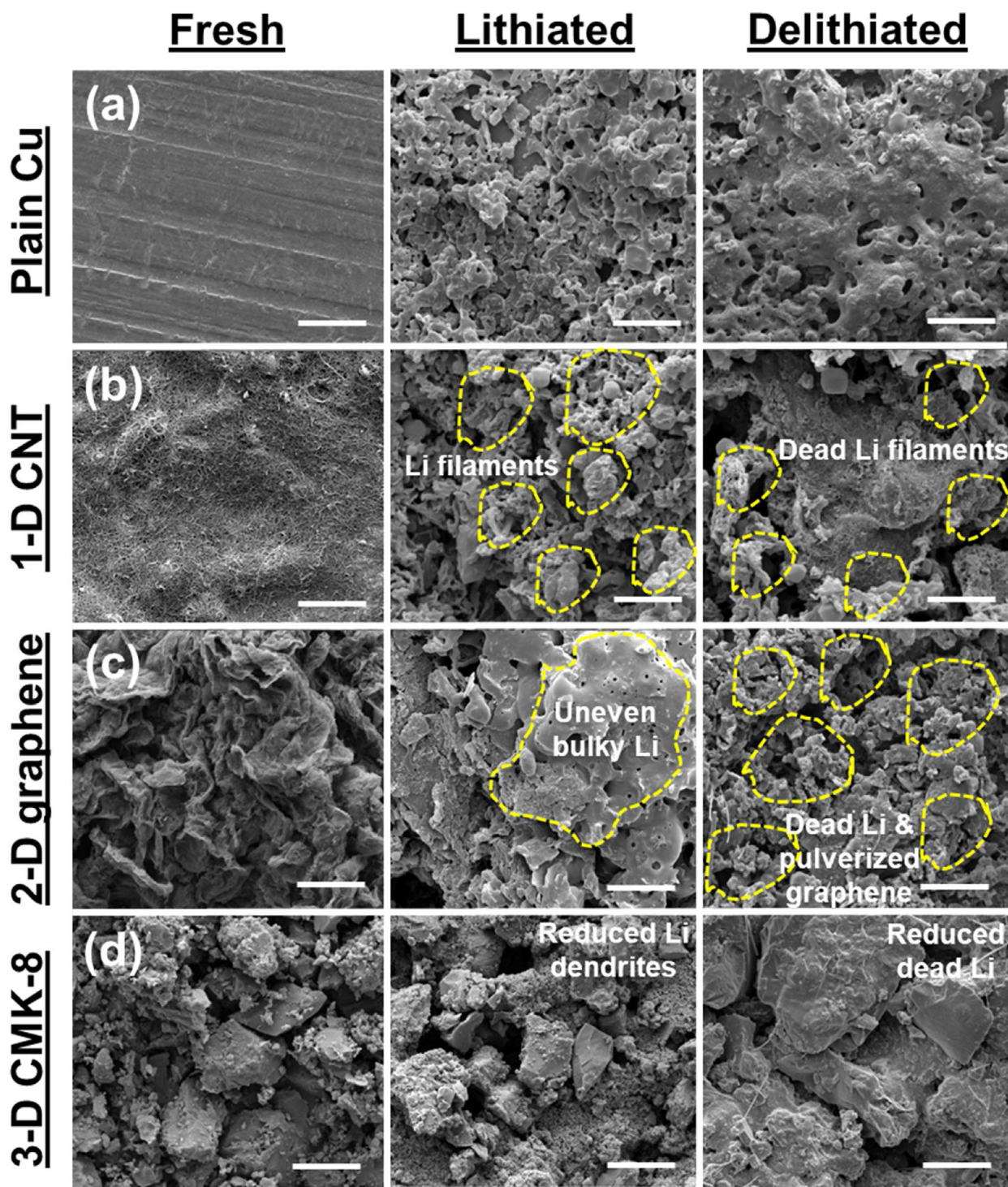
Fig. 6. SEM images of (a) plain Cu, (b) 1-D CNT, (c) 2-D graphene, and (d) 3-D CMK-8 electrodes before and after cycling for 70 times. The cycled electrodes with deposited Li (1 mA cm^{-2} for 1 mAh cm^{-2}) and after Li removal are compared. The scale bars represent 5 μm. (A colour version of this figure can be viewed online.)

compares the spectra of the CNT, graphene, and CMK-8 electrodes, respectively, before and after 70 cycles of Li plating/stripping. All the Raman spectra are characterized by a *D* band, which is associated with imperfect sp^2 carbon bonding, and a *G* band, which is related to the in-plane vibration of a well-ordered graphitic lattice [53]. It was found that the *D* band to *G* band intensity ratios (I_D/I_G) of the CNT and graphene electrodes significantly increased upon cycling, revealing an increase in defect density of the carbon hosts.

These results are in line with the SEM observation in Fig. 6. In contrast, the I_D/I_G value of the CMK-8 electrode remained unchanged after cycling. In addition, we found that for the CNT and graphene electrodes, the *D* band shifted toward a lower wavenumber and the *G* band shifted toward a higher wavenumber after cycling. These shifts are attributed to the internal stress built within the carbon structures during repeated Li plating and stripping [54]. The band shift is also associated with the formation of carbon-
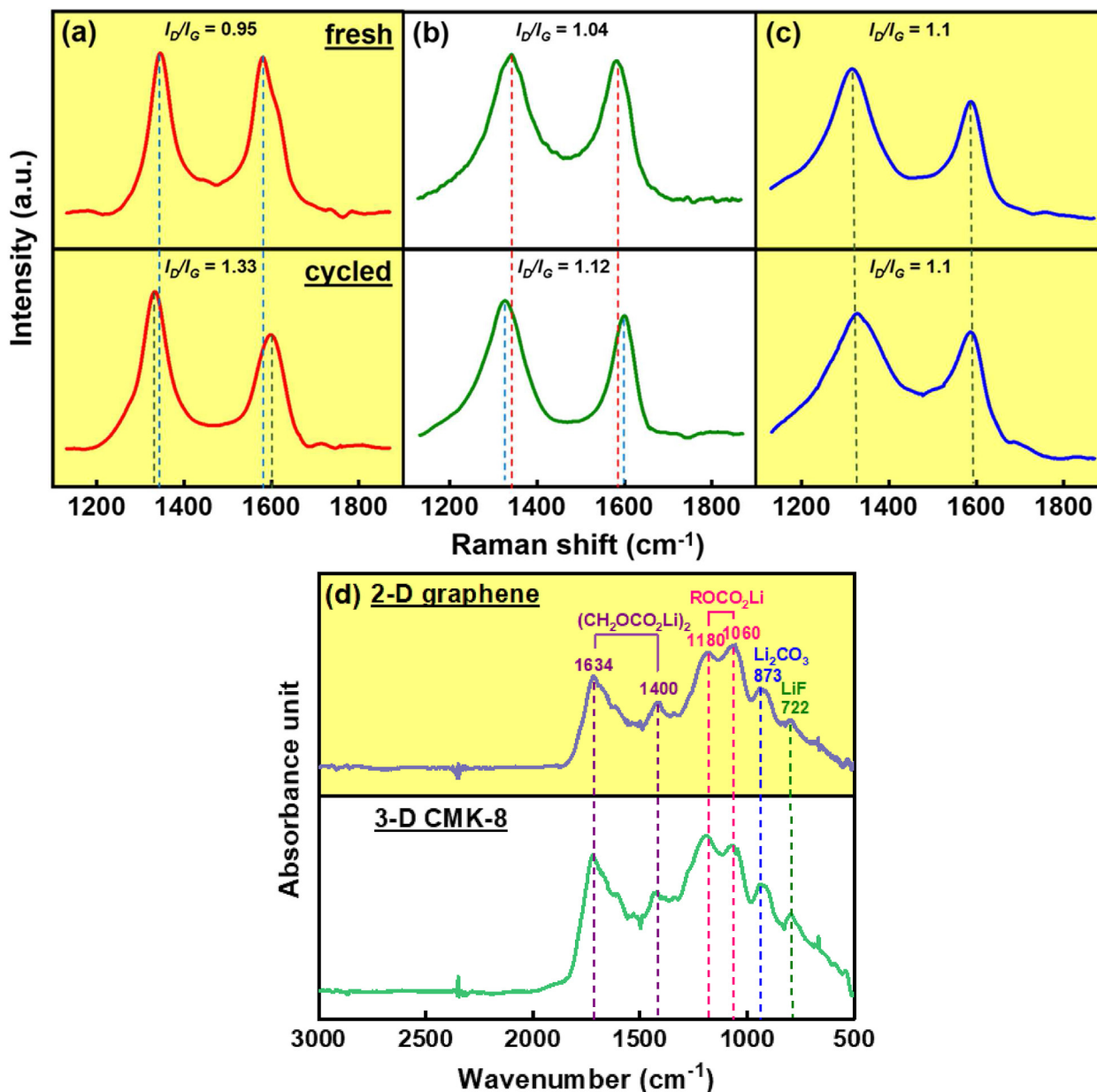
Fig. 7. Raman spectra of (a) 1-D CNT, (b) 2-D graphene, and (c) 3-D CMK-8 electrodes before and after 70 cycles of Li plating/stripping. (d) FTIR data of SEI layers formed on 2-D graphene and 3-D CMK-8 electrodes. (A colour version of this figure can be viewed online.)

related chemical bonds [55]. Because 3-D sponge-like CMK-8 is highly porous and flexible, internal stress and strain are easily released. In addition, due to the high CE and small amount of dead Li for the CMK-8 electrode, the irreversible formation of Li-carbon compounds was minimized. As a consequence, no detectable band shift was noticed for the CMK-8 electrode after cycling. These data confirm the mechanical and chemical stability of the CMK-8 electrode for LMB applications.

To examine whether the type of carbon host affects SEI chemistry, Fourier transform infrared spectroscopy (FTIR) analyses were conducted on the graphene and CMK-8 electrodes (i.e., samples with the worst and best cyclability, respectively). Fig. 7d shows the data obtained after the electrodes were cycled 70 times. As shown, the two FTIR spectra are rather similar. A LiF peak at 722 cm^{-1}, a Li_2CO_3 peak at 873 cm^{-1} [56], $ROCO_2Li$ peaks at 1060 and 1180 cm^{-1}, and $(CH_2OCO_2Li)_2$ peaks at 1400 and 1634 cm^{-1} were

observed [57]. The results reveal that the carbon architecture does not significantly alter the SEI composition. The major functions of the 3-D CMK-8 host are summarized and schematically shown in Fig. 8a. Besides the capillary effects mentioned above, the underneath Cu substrate provides high electronic conductivity. As a result, the Li deposition prefers bottom growth [58,59].

To assess the feasibility of practical battery applications, full cells were constructed using the proposed LED electrolyte and an NMC-811 cathode combined with various Li-free carbon electrodes. Before cell assembly, the CNT, graphene, and CMK-8 electrodes were conditioned in Li half cells for three Li plating/stripping cycles. Fig. 8b shows the variations of specific capacities (based on NMC-811) and CE versus the cycle number for three kinds of cells using various negative electrodes. The cells were charged and discharged at 50 mA g^{-1} within a voltage range of 2.7–4.2 V. The initial capacities of the three cells are similar (~185 mAh g^{-1}). The values
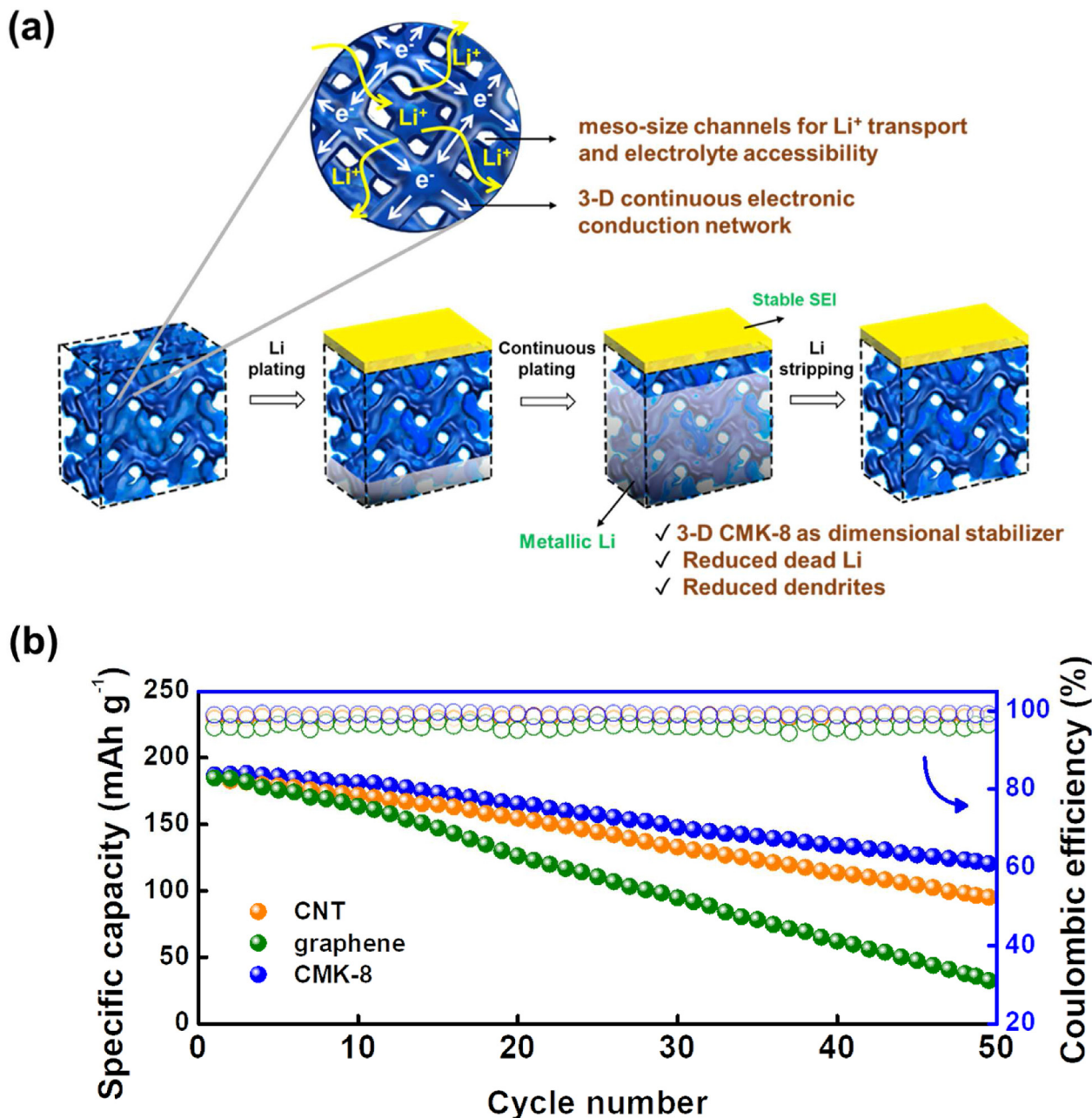
Fig. 8. (a) Schematic of major functions of 3-D CMK-8 framework for hosting Li plating/stripping. (b) Cycling stability profiles of NMC-811 full cells with various carbon host negative electrodes. (A colour version of this figure can be viewed online.)

then decrease to 96, 33, and 120 mAh g^{-1}, respectively, for the CNT, graphene, and CMK-8 cells after 50 charge-discharge cycles. These values correspond to 52%, 18%, and 66% capacity retention ratios upon cycling. The average CE values are 98.6%, 96.4%, and 99.0%, respectively. Under such harsh conditions (i.e., without Li at the initial negative electrode and using a practical current rate), the CMK-8 cell exhibited cyclability that is among the best data reported in the literature [10,60,61]. The results show that the 3-D-structure electrode exhibits great electrochemical properties and is thus a promising candidate for hosting Li plating/stripping at the anode side of high-energy-density LMBs. The results can guide the future design of the negative electrodes for LMBs. An inexpensive 3-D material needs to be developed for practical applications.

4. Conclusions

Electrolyte recipes and carbon host materials were developed for LMBs. The binary ether/carbonate LED electrolyte leads to the formation of a favorable LiF/Li$_2$CO$_3$-enriched SEI, thus improving the CE during Li plating/stripping and cyclability. Moreover, the LED electrolyte is able to withstand a high potential of ~4.45 V (vs. Li$^+$/ Li), allowing the operation of an NMC-811 cathode. This work also systematically compared 1-D CNT, 2-D graphene, and 3-D CMK-8 host materials for Li metal plating/stripping. The high surface area and 3-D continuous electronic conduction network of CMK-8 dissipate the redox current and minimize the amount of dead Li. CMK-8 also provides interpenetrating meso-size channels for

electrolyte accessibility. Because Li^+ transport is enhanced and the deposited Li is confined within the mesopores, dendritic Li formation is suppressed. The robust CMK-8 scaffold acts as a dimensional stabilizer that ensures electrode/electrolyte interface stability. We found that the CMK-8 framework is mechanically and chemically stable. The internal stress that builds up during Li plating/stripping can be easily released. No irreversible formation of Li-carbon compounds was observed. The unique properties of CMK-8 result in a superior CE of 99.2% at 1 mA cm^{-2}; moreover, great stability of up to 550 charge-discharge cycles is achievable. The potential of the developed electrolyte and 3-D carbon host material for LMB applications was demonstrated.

CRediT authorship contribution statement

Egy Adhitama: Conceptualization, Data curation, Formal analysis, Investigation, Methodology, Writing — original draft. **Purna Chandra Rath:** Formal analysis, Data curation, Methodology, Editing. **Achmad Prayogi:** Investigation, Methodology. **Jagabandhu Patra:** Data curation, Methodology. **Tai-Chou Lee:** Writing — review & editing, Review and editing, Prof. **Ju Li:** Writing — review & editing, Review and editing. **Jeng-Kuei Chang:** Conceptualization, Data curation, Review and editing, Writing — review & editing, Supervision, Funding, Resource, Funding acquisition, Resources.

Declaration of competing interest

The authors declare that they have no known competing financial interests or personal relationships that could have appeared to influence the work reported in this paper.

Acknowledgments

Appendix A. Supplementary data

Supplementary data to this article can be found online at https://doi.org/10.1016/j.carbon.2021.08.087.

References

[1] C. Zhang, Z. Huang, W. Lv, Q. Yun, F. Kang, Q.-H. Yang, Carbon enables the practical use of lithium metal in a battery, Carbon 123 (2017) 744—755.
[2] W. Xu, J. Wang, F. Ding, X. Chen, E. Nasybulin, Y. Zhang, J.G. Zhang, Lithium metal anodes for rechargeable batteries, Energy Environ. Sci. 7 (2014) 513—537.
[3] G.Y. Zheng, S.W. Lee, Z. Liang, H.W. Lee, K. Yan, H.B. Yao, H.T. Wang, W.Y. Li, S. Chu, Y. Cui, Interconnected hollow carbon nanospheres for stable lithium metal anodes, Nat. Nanotechnol. 9 (2014) 618—623.
[4] R. Zhang, X.B. Cheng, C.Z. Zhao, H.J. Peng, J.L. Shi, J.Q. Huang, J.F. Wang, F. Wei, Q. Zhang, Conductive nanostructured scaffolds render low local current density to inhibit lithium dendrite growth, Adv. Mater. 28 (2016) 2155—2162.
[5] S. Liu, A. Wang, Q. Li, J. Wu, K. Chiou, J. Huang, J. Luo, Crumpled graphene balls stabilized dendrite free lithium metal anodes, Joule 2 (2018) 184—193.
[6] W. Li, H. Yao, K. Yan, G. Zheng, Z. Liang, Y.M. Chiang, Y. Cui, The synergetic effect of lithium polysulfide and lithium nitrate to prevent lithium dendrite growth, Nat. Commun. 6 (2015) 7436.
[7] S. Huang, L. Tang, H.S. Najafabadi, S. Chen, Z. Ren, A highly flexible semitubular carbon film for stable lithium metal anodes in high-performance batteries, Nano Energy 38 (2017) 504—509.
[8] F. Wu, Y.-X. Yuan, X.-B. Cheng, Y. Bai, Y. Li, C. Wu, Q. Zhang, Perspectives for restraining harsh lithium dendrite growth: towards robust lithium metal anodes, Energy Storage Mater. 15 (2018) 148—170.
[9] H. Yang, C. Guo, A. Naveed, J. Lei, J. Yang, Y. Nuli, J. Wang, Recent progress and perspective on lithium metal anode protection, Energy Storage Mater. 14 (2018) 199—221.
[10] X.L. Fan, L. Chen, O. Borodin, X. Ji, J. Chen, S. Hou, T. Deng, J. Zheng, C.Y. Yang, S.C. Liou, K. Amine, K. Xu, C.S. Wang, Non-flammable electrolyte enables Li-

[11] Y. Jie, X. Ren, R. Cao, W. Cai, S. Jiao, Advanced liquid electrolytes for rechargeable Li metal batteries, Adv. Funct. Mater. 30 (2020) 1910777.
[12] S. Jiao, X. Ren, R. Cao, M.H. Engelhard, Y. Liu, D. Hu, D. Mei, J. Zheng, W. Zhao, Q. Li, N. Liu, B.D. Adams, C. Ma, J. Liu, J.-G. Zhang, W. Xu, Stable cycling of high-voltage lithium metal batteries in ether electrolytes, Nat. Energy 3 (2018) 739—746.
[13] X. Fan, L. Chen, X. Ji, T. Deng, S. Hou, J. Chen, J. Zheng, F. Wang, J. Jiang, K. Xu, C. Wang, Highly fluorinated interphases enable high-voltage Li-metal batteries, Inside Chem. 4 (2018) 174—185.
[14] X. Chen, X. Shen, B. Li, H.J. Peng, X.B. Cheng, B.Q. Li, X.Q. Zhang, J.Q. Huang, Q. Zhang, Ion—solvent complexes promote gas evolution from electrolytes on a sodium metal anode, Angew. Chem. Int. Ed. 57 (2018) 734—737.
[15] F. Ding, W. Xu, X. Chen, J. Zhang, M.H. Engelhard, Y. Zhang, B.R. Johnson, J.V. Crum, T.A. Blake, X. Liu, J.-G. Zhang, Effects of carbonate solvents and lithium salts on morphology and Coulombic efficiency of lithium electrode, J. Electrochem. Soc. 160 (2013) A1894—A1901.
[16] J.T. Vaughey, G. Liu, J.G. Zhang, Stabilizing the surface of lithium metal, MRS Bull. 39 (2014) 429—435.
[17] I. Epelboin, M. Froment, M. Garreau, J. Thevenin, D. Warin, Behavior of secondary lithium and aluminum-lithium electrodes in propylene carbonate, J. Electrochem. Soc. 127 (1980) 2100—2104.
[18] C. Brissot, M. Rosso, J.N. Chazalviel, S. Lascaud, Dendritic growth mechanisms in lithium/polymer cells, J. Power Sources 81 (1999) 925—929.
[19] J.M. Tarascon, M. Armand, Issues and challenges facing rechargeable lithium batteries, Nature 414 (2001) 359—367.
[20] X.B. Cheng, R. Zhang, C.Z. Zhao, Q. Zhang, Toward safe lithium metal anode in rechargeable batteries: A review, Chem. Rev. 117 (2017) 10403—10473.
[21] C.C. Fang, J.X. Li, M.H. Zhang, Y.H. Zhang, F. Yang, J.Z. Lee, M.H. Lee, J. Alvarado, M.A. Schroeder, Y.Y.C. Yang, B.Y. Lu, N. Williams, M. Ceja, L. Yang, M. Cai, J. Gu, K. Xu, X.F. Wang, Y.S. Meng, Quantifying inactive lithium in lithium metal batteries, Nature 572 (2019) 511—515.
[22] H. Ye, S. Xin, Y.X. Yin, Y.G. Guo, Advanced porous carbon materials for high-efficient lithium metal anodes, Adv. Energy Mater. 7 (2017) 1700530.
[23] J.S. Kim, D.W. Kim, H.T. Jung, J.W. Choi, Controlled lithium dendrite growth by a synergistic effect of multilayered graphene coating and an electrolyte additive, Chem. Mater. 27 (2015) 2780—2787.
[24] A.R.O. Raji, R.V. Salvatierra, N.D. Kim, X. Fan, Y. Li, G.A.L. Silva, J. Sha, J.M. Tour, Lithium batteries with nearly maximum metal storage, ACS Nano 11 (2017) 6362—6369.
[25] Y. Xu, X. Zhu, X. Zhou, X. Liu, Y. Liu, Z. Dai, J. Bao, Ge nanoparticles encapsulated in nitrogen-doped reduced graphene oxide as an advanced anode material for lithium-ion batteries, J. Phys. Chem. C 118 (2014) 28502—28508.
[26] J. Han, D. Kong, W. Lv, D.M. Tang, D. Han, C. Zhang, D. Liu, Z. Xiao, X. Zhang, J. Xiao, X. He, F.C. Hsia, C. Zhang, Y. Tao, D. Golberg, F. Kang, L. Zhi, Q.H. Yang, Caging tin oxide in three-dimensional graphene networks for superior volumetric lithium storage, Nat. Commun. 9 (2018) 402.
[27] T.T. Zuo, Y.X. Yin, S.H. Wang, P.F. Wang, X. Yang, J. Liu, C.P. Yang, Y.G. Guo, Trapping lithium into hollow silica microspheres with a carbon nanotube core for dendrite-free lithium metal anodes, Nano Lett. 18 (2018) 297—301.
[28] H. Chen, A. Pei, J. Wan, D. Lin, R. Vilá, H. Wang, D. Mackanic, H.-G. Steinrück, W. Huang, Y. Li, A. Yang, J. Xie, Y. Wu, H. Wang, Y. Cui, Tortuosity effects in lithium-metal host anodes, Joule 4 (2020) 938—952.
[29] J. Patra, P.C. Rath, C.H. Yang, D. Saikia, H.M. Kao, J.K. Chang, Three-dimensional interpenetrating mesoporous carbon confining SnO_2 particles for superior sodiation/desodiation properties, Nanoscale 9 (2017) 8674—8683.
[30] C.H. Wu, C.H. Wang, M.T. Lee, J.K. Chang, Unique Pd/graphene nanocomposites constructed using supercritical fluid for superior electrochemical sensing performance, J. Mater. Chem. 22 (2012) 21466—21471.
[31] J. Zheng, J.A. Lochala, A. Kwok, Z.D. Deng, J. Xiao, Research progress towards understanding the unique interfaces between concentrated electrolytes and electrodes for energy storage applications, Adv. Sci. 4 (2017) 1700032.
[32] J. Zheng, X. Fan, G. Ji, H. Wang, S. Hou, K.C. DeMella, S.R. Raghavan, J. Wang, K. Xu, C. Wang, Manipulating electrolyte and solid electrolyte interphase to enable safe and efficient Li-S batteries, Nano Energy 50 (2018) 431—440.
[33] D. Aurbach, E. Zinigrad, H. Teller, P. Dan, Factors which limit the cycle life of rechargeable lithium (metal) batteries, J. Electrochem. Soc. 147 (2000) 1274—1279.
[34] X. Nie, A. Zhang, Y. Liu, C. Shen, M. Chen, C. Xu, Q. Liu, J. Cai, A. Alfaraidi, C. Zhou, Synthesis of interconnected graphene framework with two-dimensional protective layers for stable lithium metal anodes, Energy Storage Mater. 17 (2019) 341—348.
[35] S.J. Yang, N. Yao, X.Q. Xu, F.N. Jiang, X. Chen, H. Liu, H. Yuan, J.Q. Huang, X.B. Cheng, Formation mechanism of the solid electrolyte interphase in different ester electrolytes, J. Mater. Chem. A (2021), https://doi.org/10.1039/d1ta02615a.
[36] T. Liu, L. Lin, X. Bi, L. Tian, K. Yang, J. Liu, M. Li, Z. Chen, J. Lu, K. Amine, K. Xu, F. Pan, In situ quantification of interphasial chemistry in Li-ion battery, Nat. Nanotechnol. 14 (2019) 50—56.
[37] H. Zheng, H. Xiang, F. Jiang, Y. Liu, Y. Sun, X. Liang, Y. Feng, Y. Yu, Lithium difluorophosphate-based dual-salt low concentration electrolytes for lithium metal batteries, Adv. Energy Mater. 10 (2020) 2001440.
[38] S. Xiong, S. Diao, X. Hong, Y. Chen, K. Xie, Characterization of solid electrolyte interphase on lithium electrodes cycled in ether-based electrolytes for lithium

batteries, J. Electroanal. Chem. 719 (2014) 122–126.

[39] S.Y. Lee, Y.J. Park, Effect of vinylethylene carbonate and fluoroethylene carbonate electrolyte additives on the performance of lithia-based cathodes, ACS Omega 5 (2020) 3579–3587.

[40] H.B. Son, M.-Y. Jeong, J.-G. Han, K. Kim, K.H. Kim, K.-M. Jeong, N.-S. Choi, Effect of reductive cyclic carbonate additives and linear carbonate co-solvents on fast chargeability of $LiNi_{0.6}Co_{0.2}Mn_{0.2}O_2$/graphite cells, J. Power Sources 400 (2018) 147–156.

[41] H.-H. Sun, A. Dolocan, J.A. Weeks, R. Rodriguez, A. Heller, C.B. Mullins, In-situ formation of a multicomponent inorganic-rich SEI layer provides a fast charging and high specific energy Li-metal battery, J. Mater. Chem. A 7 (2019) 17782–17789.

[42] N. Takenaka, Y. Suzuki, H. Sakai, M. Nagaoka, On electrolyte-dependent formation of solid electrolyte interphase film in lithium-ion batteries: strong sensitivity to small structural difference of electrolyte molecules, J. Phys. Chem. C 118 (2014) 10874–10882.

[43] S.K. Heiskanen, J. Kim, B.L. Lucht, Generation and evolution of the solid electrolyte interphase of lithium-ion batteries, Joule 3 (2019) 2322–2333.

[44] M. Lu, H. Cheng, Y. Yang, A comparison of solid electrolyte interphase (SEI) on the artificial graphite anode of the aged and cycled commercial lithium ion cells, Electrochim. Acta 53 (2008) 3539–3546.

[45] G.G. Eshetu, T. Diemant, S. Grugeon, R.J. Behm, S. Laruelle, M. Armand, S. Passerini, In-depth interfacial chemistry and reactivity focused investigation of lithium–imide and lithium–imidazole-based electrolytes, ACS Appl. Mater. Interfaces 8 (2016) 16087–16100.

[46] Q. Zhang, J. Pan, P. Lu, Z. Liu, M.W. Verbrugge, B.W. Sheldon, Y.T. Cheng, Y. Qi, X. Xiao, Synergetic effects of inorganic components in solid electrolyte interphase on high cycle efficiency of lithium ion batteries, Nano Lett. 16 (2016) 2011–2016.

[47] J.F. Qian, B.D. Adams, J.M. Zheng, W. Xu, W.A. Henderson, J. Wang, M.E. Bowden, S.C. Xu, J.Z. Hu, J.G. Zhang, Anode-free rechargeable lithium metal batteries, Adv. Funct. Mater. 26 (2016) 7094–7102.

[48] Y.Y. Lu, Z.Y. Tu, L.A. Archer, Stable lithium electrodeposition in liquid and nanoporous solid electrolytes, Nat. Mater. 13 (2014) 961–969.

[49] X. Ren, L. Zou, S. Jiao, D. Mei, M.H. Engelhard, Q. Li, H. Lee, C. Niu, B.D. Adams, C. Wang, J. Liu, J.-G. Zhang, W. Xu, High-concentration ether electrolytes for stable high-voltage lithium metal batteries, ACS Energy Lett. 4 (2019) 896–902.

[50] Z. Wang, X. Li, Y. Chen, K. Pei, Y.-W. Mai, S. Zhang, J. Li, Creep-enabled 3D solid-state lithium-metal battery, Inside Chem. 6 (2020) 2878–2892.

[51] J. Yan, M. Liu, N. Deng, L. Wang, A. Sylvestre, W. Kang, Y. Zhao, Flexible MnO nanoparticle-anchored N-doped porous carbon nanofiber interlayers for superior performance lithium metal anodes, Nanoscale Adv. 3 (2021) 1136–1147.

[52] G. Jiang, N. Jiang, N. Zheng, X. Chen, J. Mao, G. Ding, Y. Li, F. Sun, Y. Li, MOF-derived porous Co_3O_4-NC nanoflake arrays on carbon fiber cloth as stable hosts for dendrite-free Li metal anodes, Energy Storage Mater. 23 (2019) 181–189.

[53] K.N. Kudin, B. Ozbas, H.C. Schniepp, R.K. Prud'homme, I.A. Aksay, R. Car, Raman spectra of graphite oxide and functionalized graphene sheets, Nano Lett. 8 (2008) 36–41.

[54] G. Choi, J. Kim, B. Kang, Understanding limited reversible capacity of a SiO electrode during the first cycle and its effect on initial Coulombic efficiency, Chem. Mater. 31 (2019) 6097–6104.

[55] F. Wan, H. Shi, W. Chen, Z. Gu, L. Du, P. Wang, J. Wang, Y. Huang, Charge transfer effect on Raman and surface enhanced Raman spectroscopy of furfural molecules, Nanomaterials 7 (2017) 210.

[56] E. Markevich, G. Salitra, F. Chesneau, M. Schmidt, D. Aurbach, Very stable lithium metal stripping–plating at a high rate and high areal capacity in fluoroethylene carbonate-based organic electrolyte solution, ACS Energy Lett. 2 (2017) 1321–1326.

[57] P. Verma, P. Maire, P. Novák, A review of the features and analyses of the solid electrolyte interphase in Li-ion batteries, Electrochim. Acta 55 (2010) 6332–6341.

[58] J. Yun, B.K. Park, E.S. Won, S.H. Choi, H.C. Kang, J.H. Kim, M.S. Park, J.W. Lee, Bottom-up lithium growth triggered by interfacial activity gradient on porous framework of lithium-metal anode, ACS Energy Lett. 5 (2020) 3108–3114.

[59] J. Lee, E.S. Won, D.M. Kim, H. Kim, B. Kwon, K. Park, S. Jo, S. Lee, J.W. Lee, K.T. Lee, Three-dimensional porous frameworks for Li metal batteries: Super conformal versus conformal Li growth, ACS Appl. Mater. Interfaces 13 (2021) 33056–33065.

[60] N.A. Sahalie, Z.T. Wondimkun, W.-N. Su, M.A. Weret, F.W. Fenta, G.B. Berhe, C.J. Huang, Y.-C. Hsu, B.J. Hwang, Multifunctional properties of Al2O3/poly-acrylonitrile composite coating on Cu to suppress dendritic growth in anode-free Li-metal battery, ACS Appl. Energy Mater. 3 (2020) 7666–7679.

[61] B.A. Jote, T.T. Beyene, N.A. Sahalie, M.A. Weret, B.W. Olbassa, Z.T. Wondimkun, G.B. Berhe, C.-J. Huang, W.N. Su, B.J. Hwang, Effect of diethyl carbonate solvent with fluorinated solvents as electrolyte system for anode free battery, J. Power Sources 461 (2020) 228102.